

## Ayaz Siddiqui

Department of Mechanical and  
Aerospace Engineering,  
North Carolina State University,  
Raleigh, NC 27606  
e-mail: asiddiq2@ncsu.edu

## Kartik Naik

Department of Mechanical and  
Aerospace Engineering,  
North Carolina State University,  
Raleigh, NC 27606  
e-mail: knaik@ncsu.edu

## Mitchell Cobb

Department of Mechanical and  
Aerospace Engineering,  
North Carolina State University,  
Raleigh, NC 27606  
e-mail: mcobb@ncsu.edu

## Kenneth Granlund

Assistant Professor  
Department of Mechanical and  
Aerospace Engineering,  
North Carolina State University,  
Raleigh, NC 27606  
e-mail: kgranlu@ncsu.edu

## Chris Vermillion<sup>1</sup>

Associate Professor,  
Department of Mechanical and  
Aerospace Engineering,  
North Carolina State University,  
Raleigh, NC 27606  
e-mail: cvermil@ncsu.edu

# Lab-Scale, Closed-Loop Experimental Characterization, Model Refinement, and Validation of a Hydrokinetic Energy-Harvesting Ocean Kite

*This paper presents a study wherein we experimentally characterize the dynamics and control system of a lab-scale ocean kite, and then refine, validate, and extrapolate this model for use in a full-scale system. Ocean kite systems, which harvest tidal and ocean current resources through high-efficiency cross-current motion, enable energy extraction with an order of magnitude less material (and cost) than stationary systems with the same rated power output. However, an ocean kite represents a nascent technology that is characterized by relatively complex dynamics and requires sophisticated control algorithms. In order to characterize the dynamics and control of ocean kite systems rapidly, at a relatively low cost, the authors have developed a lab-scale, closed-loop prototyping environment for characterizing tethered systems, whereby 3D printed systems are tethered and flown in a water channel environment. While this system has been shown to be capable of yielding similar dynamic characteristics to some full-scale systems, there are also fundamental limitations to the geometric scales and flow speeds within the water channel environment, making many other real-world scenarios impossible to replicate from the standpoint of dynamic similarity. To address these scenarios, we show how the lab-scale framework is used to refine and validate a scalable dynamic model of a tethered system, which can then be extrapolated to full-scale operation. In this work, we present an extensive case study of this model refinement, validation, and extrapolation on an ocean kite system intended for operation in the Gulf Stream or similar current environments. [DOI: 10.1115/1.4047825]*

## 1 Introduction

High-altitude winds routinely possess 5–8 times the power density of ground-level winds [1], whereas the Agulhas Current off the coast of South Africa and the Gulf Stream possess energy potentials of about 1913 GWh and 219 GWh per year, respectively [2,3]. The limitations of towered turbines and fixed-base marine hydrokinetic energy devices in harnessing these vast sources of energy has led to the development of tethered energy systems over the past decade, where the structural elements of the tower are replaced with tethers and lifting bodies.

Figure 1 shows systems originating from Minesto, Ltd.,<sup>2</sup> Windlift, Inc.,<sup>3</sup> and Makani Power,<sup>4</sup> which give an indication of the diversity in design of tethered energy systems. Broadly speaking these systems can be grouped into two categories:

- (1) *On-board power generation*, which consist of turbine(s) attached to the lifting body (termed the “kite”) that transmit energy to a base station via a conductive tether [4–6].<sup>3,4</sup>
- (2) *Ground-based systems*, such as those developed by the method given online,<sup>5</sup> utilize a motor/generator attached to

a winch which spools out tether under high tension and spools in tether under low tension, resulting in net positive energy.

All of the aforementioned systems are designed to execute power-augmenting cross-current motion (high-speed figure-8 or circular patterns perpendicular to the prevailing flow) to increase the apparent flow presented to the system, thereby substantially increasing power generation [7]. There exists a substantial amount of simulation-driven research on the closed-loop dynamics of these systems, utilizing physics-based dynamic models [8–12]. Due to the early stage and often simplifying nature of the aforementioned models, significant attention has been given to small-scale experimental validation, particularly over the past decade. For example, the authors of Ref. [13] built an approximately 30 m line length system for optimizing figure-8 crosswind motions of airborne wind energy systems. A pool-scale tow testing platform that examined several attributes of tethered undersea kite performance was evaluated in Ref. [14]. The authors of Refs. [15–19], on the other hand, developed a lab-scale framework wherein 3D printed models of tethered systems were flown in a water channel environment. References [15] and [16] proposed an initial framework for measuring position and orientation of a lab-scale system during passive operation. This was followed by several closed-loop characterizations in Refs. [17], [19], and [20]. In fact, for a specific tethered energy system (a buoyant airborne wind energy system), Refs. [18] and [20] derived and validated conditions for the dynamic similarity of lab-scale and full-scale dynamics.

<sup>1</sup>Corresponding author.

<sup>2</sup><https://www.minesto.com>

<sup>3</sup><http://www.windlift.com>

<sup>4</sup><http://www.makanipower.com>

<sup>5</sup><http://www.ampyxpower.com>

Contributed by the Dynamic Systems Division of ASME for publication in the JOURNAL OF DYNAMIC SYSTEMS, MEASUREMENT, AND CONTROL. Manuscript received March 8, 2020; final manuscript received July 10, 2020; published online August 7, 2020. Assoc. Editor: Mohammad A. Youbi.



**Fig. 1 Tethered energy systems adapted from Minesto, Ltd. (left), Windlift, Inc. (middle), and Makani Power (right)**

While the aforementioned small-scale experimental platforms have led to tremendous advancements in the design and control of tethered energy systems, there have been very limited efforts to use those small-scale platforms to refine physics-driven models of these systems. The present work focuses specifically on the use of the aforementioned lab-scale, water channel-based platform to systematically refine a scalable physics-driven dynamic model of an ocean kite system and then extrapolate these results to predict full-scale dynamic behavior. This effort is important for two reasons:

- (1) An accurate dynamic model is invaluable for refining and optimizing the designs of tethered energy systems. Thus, the systematic use of the experimental framework to refine the model can serve as a major aid in design refinement and optimization.
- (2) Several practical considerations make it impossible, in certain circumstances, to achieve exact dynamic similarity between lab-scale and full-scale dynamic behavior.

This work focuses on an ocean kite system designed to yield approximately 100 kW of power output in a 2 m/s flow speed, which is intended to operate at full scale with over 100 meters of tether length, using on-board control surfaces to follow high-performance cross-current motion paths. The optimization of the physical system design and corresponding control system demand an accurate dynamic model, and lab-scale experiments serve an instrumental role in informing that model. Furthermore, practical constraints on the water channel environment preclude exact dynamic similarity between lab-scale and full-scale operation for several reasons:

- (1) Exact dynamic similarity requires hydrodynamic coefficients to be consistent at both lab scale and full scale. This will not be possible for the targeted ocean kite geometry due to the Reynolds numbers seen at lab scale.
- (2) Geometric limitations of the water channel mean that we cannot create dynamically similar performance to a kite system with a tether length greater than 100 m, thereby precluding us from emulating the most efficient cross-current motion.
- (3) Control via the use of hydrodynamic control surfaces is infeasible for a lab-scale model due to size constraints.

In light of these considerations, this paper focuses on refining and validating a scalable dynamic model at lab scale, using hydrodynamic coefficients calculated at Reynolds numbers seen in the water channel, then scaling the ocean kite to full-scale and recalculating the hydrodynamic coefficients at the appropriate Reynolds numbers. We use these coefficients to simulate the full-scale system. In summary, the contributions of this paper are as follows:

- (1) The first demonstration of closed-loop cross-current motion at lab scale for an ocean kite;

- (2) The first quantification of model accuracy through calculation of root mean squared errors between model predictions and measured values for an ocean kite;
- (3) Extrapolation of lab-scale design to full-scale operation.

The remainder of the paper is organized as follows. Section 2 provides an overview of the full-scale and the lab-scale systems. The dynamic model and the control strategies for the full-scale and the lab-scale system are detailed in Secs. 3 and 4, respectively. An overview of the experimental measurement system is provided in Sec. 5. Section 6 details the model refinement and validation methodologies used, followed by refinement results presented in Sec. 7. The extrapolation of the lab-scale design to full scale and the corresponding results are presented in Sec. 8.

## 2 Kite Design Fundamentals

In this section, we provide an overview of the intended full-scale ocean kite system and its lab-scale counterpart, while simultaneously highlighting the key differences between them.

**2.1 Full-Scale System.** The full-scale ocean kite system consists of a kite connected to the base station via a single flexible tether as shown in Fig. 2. The nominal kite used in this work has a wing span of 10 m and a nose-to-tail length of 9 m. This kite is designed to execute cross-current motion by making use of a path-following controller presented in Sec. 4. Control over the roll, pitch, and yaw angles is achieved through the actuation of control surfaces. Depth control is achieved by trimming to a suitable angle of attack and spooling the tether. The relevant states of the system are measured by making use of an inertial measurement unit (IMU) and other auxiliary equipment mounted on-board.

**2.2 Lab-Scale System.** The lab-scale system consists of a 15/1000-scale 3D printed model of the full-scale kite, three tethers, and a motion capture system. The kite has a wing span of 15 cm and a nose-to-tail length of 13.5 cm. Although the full-scale kite is controlled using active control surfaces, its lab-scale counterpart is controlled via the actuation of the three tethers as it is infeasible to fabricate a prototype this small with active control surfaces. The booms on the wingtips are added to trim at suitable pitch angles prior to initiation of induced cross-current motion. Measurement of the relevant states is performed via a motion capture system, as it is infeasible to mount an IMU or other equipment on the lab-scale prototype. Figure 3 shows a schematic of the lab-scale experimental setup.

## 3 Dynamic Model

The dynamic modeling described in this paper is based on Ref. [21], which uses a classical Newton–Euler formulation to derive the governing equations for an array of tethered ocean current

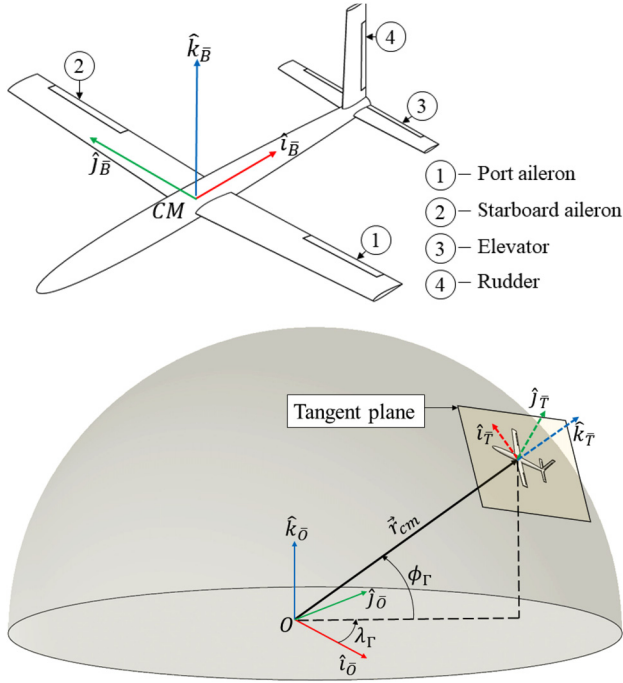


**Fig. 2** Schematic of the full-scale kite showing the body-fixed frame,  $\bar{B}$ , the various control surfaces (top), the inertial frame,  $\bar{O}$ , and the tangent frame,  $\bar{T}$

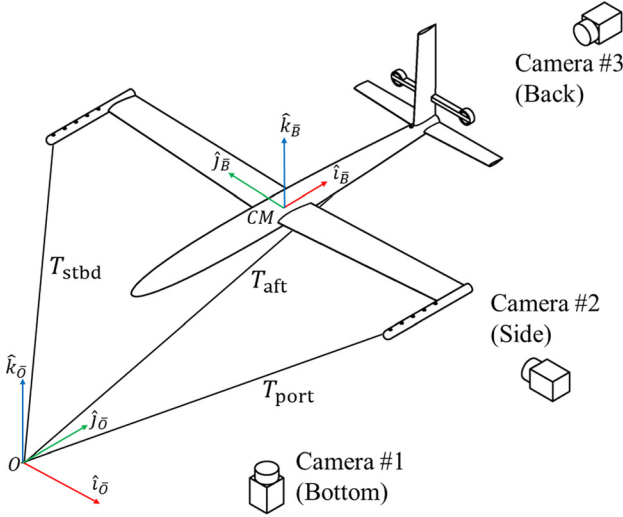


**Fig. 3** Schematic of the experimental setup showing the lab-scaled kite model, tethers ( $T_{port}$ ,  $T_{stbd}$ , and  $T_{aft}$ ), camera locations, the inertial frame,  $\bar{O}$ , and the body-fixed frame,  $\bar{B}$

turbines. This model is highly flexible and can be used to simulate the full-scale system, which utilizes a single tether, active control surfaces, and operates at higher Reynolds number; as well as the lab-scale system, which makes use of three tethers, and operates at low Reynolds numbers.

**3.1 Kite Model.** The six degrees-of-freedom kite model is created to characterize the dynamic behavior of the ocean kite and aid in the development of suitable cross-current motion control methodologies. The kite is modeled as a rigid body attached to a base station by elastic tethers. The kite dynamics are driven by gravity, buoyancy, hydrodynamic, and tether forces.

**3.1.1 Reference Frames and Kinematics.** In order to derive the equations of motion of the system, an inertial frame ( $\bar{O}$ ), a

body-fixed frame ( $\bar{B}$ ), and a tangent frame ( $\bar{T}$ ) are needed to define the position and orientation of the kite. The inertial frame is situated at the origin, with its  $y$ -axis pointing in the downstream direction and its  $z$ -axis pointing upward, while the  $x$ -axis is obtained by simply applying the right hand rule. The body-fixed frame is situated at the center of mass of the kite, with its  $x$ -axis pointing toward the tail, the  $y$ -axis pointing toward the starboard wing, and the  $z$ -axis pointing upward. The tangent frame, which is used as a reference frame for path tracking, is also situated at the center of mass of the kite, with its  $x$ -axis pointing toward  $\mathbf{k}_{\bar{O}}$ , and the  $z$ -axis pointing away from the origin. Diagrammatic representations of the reference frames are shown in Figs. 2 and 3.

Vectors are transformed from the inertial to body-fixed frame by premultiplying the inertial vector by the orthogonal matrix  ${}^{\bar{B}}[C]^{\bar{O}}$ . The method chosen by Fossen [22], using Euler angles with three successive rotations about the  $z$ -axis ( $\psi$ -yaw), the new  $y$ -axis ( $\theta$ -pitch), and the new  $x$ -axis ( $\phi$ -roll), are adopted as follows:

$${}^{\bar{B}}[C]^{\bar{O}} = \begin{bmatrix} C_\theta C_\psi & C_\theta S_\psi & -S_\theta \\ C_\psi S_\theta S_\phi - C_\phi S_\psi & C_\phi C_\psi + S_\theta S_\phi S_\psi & C_\theta S_\phi \\ C_\phi C_\psi S_\theta + S_\phi S_\psi & -C_\psi S_\phi + C_\phi S_\theta S_\psi & C_\theta C_\phi \end{bmatrix} \quad (1)$$

Here,  $C_\theta = \cos \theta$  and  $S_\theta = \sin \theta$ .

**3.1.2 Equations of Motion.** Using a Newton–Euler approach [23,24], a set of 12 first-order ordinary differential equations describing the dynamics of the kite can be derived. Here, the 12 state variables consist of the position of the center of mass of the system ( $\mathbf{r}_{cm} \triangleq [x_{cm} \ y_{cm} \ z_{cm}]^T$ ) in the  $\mathbf{i}_{\bar{O}}$ ,  $\mathbf{j}_{\bar{O}}$ , and  $\mathbf{k}_{\bar{O}}$  directions, the corresponding three inertial velocities of the center of mass ( $\mathbf{v}_{cm} \triangleq [u \ v \ w]^T$ ) in the  $\mathbf{i}_{\bar{B}}$ ,  $\mathbf{j}_{\bar{B}}$ , and  $\mathbf{k}_{\bar{B}}$  directions, the three Euler angles ( $\boldsymbol{\mu} \triangleq [\phi \ \theta \ \psi]^T$ ), and the three angular velocities ( $\boldsymbol{\omega} \triangleq [\omega_x \ \omega_y \ \omega_z]^T$ ) of the body-fixed frame with respect to the inertial frame. The differential equations dictating the evolution of the aforementioned state variables are as follows:

$$\dot{\mathbf{r}}_{cm} = {}^{\bar{O}}[C]^{\bar{B}} \mathbf{v}_{cm} \quad (2)$$

$$\begin{Bmatrix} \dot{\phi} \\ \dot{\theta} \\ \dot{\psi} \end{Bmatrix} = \begin{bmatrix} 1 & \sin(\phi)\tan(\theta) & \cos(\phi)\tan(\theta) \\ 0 & \cos(\phi) & -\sin(\phi) \\ 0 & \sin(\phi)\sec(\theta) & \cos(\phi)\sec(\theta) \end{bmatrix} \begin{Bmatrix} \omega_x \\ \omega_y \\ \omega_z \end{Bmatrix} \quad (3)$$

$$\begin{Bmatrix} \dot{u} \\ \dot{v} \\ \dot{w} \end{Bmatrix} = \mathbf{M}^{-1} \begin{Bmatrix} \mathbf{F}_{ext} \cdot \mathbf{i}_{\bar{B}} \\ \mathbf{F}_{ext} \cdot \mathbf{j}_{\bar{B}} \\ \mathbf{F}_{ext} \cdot \mathbf{k}_{\bar{B}} \end{Bmatrix} - \begin{Bmatrix} w\omega_x - v\omega_z \\ u\omega_z - w\omega_x \\ v\omega_x - u\omega_y \end{Bmatrix} \quad (4)$$

$$\begin{Bmatrix} \dot{\omega}_x \\ \dot{\omega}_y \\ \dot{\omega}_z \end{Bmatrix} = \begin{bmatrix} I_{xx} & 0 & 0 \\ 0 & I_{yy} & 0 \\ 0 & 0 & I_{zz} \end{bmatrix}^{-1} \begin{Bmatrix} \mathbf{M}_{cm} \cdot \mathbf{i}_{\bar{B}} + (I_{yy} - I_{zz})\omega_y\omega_z \\ \mathbf{M}_{cm} \cdot \mathbf{j}_{\bar{B}} + (I_{zz} - I_{xx})\omega_x\omega_z \\ \mathbf{M}_{cm} \cdot \mathbf{k}_{\bar{B}} + (I_{xx} - I_{yy})\omega_x\omega_y \end{Bmatrix} \quad (5)$$

Here,  $\mathbf{F}_{ext}$  and  $\mathbf{M}_{cm}$  are the sums of all external forces and moments acting on the kite, respectively.  $I_{xx}$ ,  $I_{yy}$ , and  $I_{zz}$  are the kite's principal moments of inertia. The variable  $\mathbf{M}$  is the mass matrix, which is the sum of the mass of the kite,  $m$ , and the added mass in the  $\mathbf{i}_{\bar{B}}$ ,  $\mathbf{j}_{\bar{B}}$ , and  $\mathbf{k}_{\bar{B}}$  directions. The added mass terms, denoted by  $m_{a,x}$ ,  $m_{a,y}$ , and  $m_{a,z}$  are estimated by assuming the kite to be made of simple geometric shapes like ellipsoids and flat plates, and then using the relations provided in Ref. [25] as follows:

$$\mathbf{M} = \mathbf{I}_3 m + \begin{bmatrix} m_{a,x} & 0 & 0 \\ 0 & m_{a,y} & 0 \\ 0 & 0 & m_{a,z} \end{bmatrix} \quad (6)$$

$$m_{a,x} = \pi\rho \left( b_w \left( \frac{t_w}{2} \right)^2 + b_{hs} \left( \frac{t_{hs}}{2} \right)^2 + b_{vs} \left( \frac{t_{vs}}{2} \right)^2 \right) \quad (7)$$

$$m_{a,y} = \pi\rho \left( 2.2t_w \left( \frac{c_w}{2} \right)^2 + 2.2t_{hs} \left( \frac{c_{hs}}{2} \right)^2 + b_{vs} \left( \frac{c_{vs}}{2} \right)^2 \right) \quad (8)$$

$$m_{a,z} = \pi\rho \left( b_w \left( \frac{c_w}{2} \right)^2 + b_{hs} \left( \frac{c_{hs}}{2} \right)^2 + 1.98b_{vs} \left( \frac{c_{vs}}{2} \right)^2 \right) \quad (9)$$

**3.1.3 External Loads.** The net external force vector acting on the center of mass of the kite is the sum of forces due to buoyancy, gravity, hydrodynamic lift and drag resulting from four fluid dynamic surfaces (a port wing, starboard wing, horizontal stabilizer, and vertical stabilizer), and tether tensions, given as follows:

$$\begin{aligned} \mathbf{F}_{\text{ext}} &= \mathbf{F}_B + \mathbf{F}_G + \sum_{i=1}^4 \mathbf{F}_{L,i} + \sum_{i=1}^4 \mathbf{F}_{D,i} + \mathbf{F}_T \\ &= \rho V g \mathbf{k}_O - m g \mathbf{k}_O + A_r \sum_{i=1}^4 q_i C_{L,i} \mathbf{u}_{L,i} \\ &\quad + A_r \sum_{i=1}^4 q_i C_{D,i} \mathbf{u}_{D,i} + \sum_{j=1}^{n_{\text{thr}}} \mathbf{F}_{\text{thr},j} \end{aligned} \quad (10)$$

Here,  $V$  is the volume of the kite,  $g$  is the gravitational acceleration,  $A_r$  is the reference area,  $n_{\text{thr}}$  is the number of tethers, and  $\mathbf{F}_{\text{thr},j}$  is the force exerted by tether  $j$  on the kite. The index,  $i$ , refers to each of the four independent fluid dynamic surfaces. The resulting fluid dynamic force depends on the dynamic pressure, which in turn is dependent on the apparent flow at the hydrodynamic center of each surface, and is given by

$$\begin{aligned} q_i &= \frac{1}{2} \rho \|\mathbf{v}_{a,i}\|^2 \\ &= \frac{1}{2} \rho \|\mathbf{v}_f - (\mathbf{v}_{\text{cm}} + \boldsymbol{\omega} \times \mathbf{r}_{a,i})\|^2 \end{aligned} \quad (11)$$

where  $\mathbf{v}_f$  is the flow velocity and  $\mathbf{r}_{a,i}$  is the vector from the center of mass of the kite to the hydrodynamic center of the  $i$ th surface. The fluid dynamic coefficients ( $C_{L,i}$  and  $C_{D,i}$ ), which are dependent on the Reynolds number experienced at a given scale, are obtained by modeling each fluid dynamic surface independently in the XFOIL software [26], then applying a standard correction to account for lift-induced drag. Lastly,  $\mathbf{u}_{D,i}$  and  $\mathbf{u}_{L,i}$  are unit vectors pointing in the direction of the drag and lift force of the  $i$ th hydrodynamic surface. Here,  $\mathbf{u}_{D,i}$  acts in the direction parallel to the apparent flow  $\mathbf{v}_{a,i}$ , whereas  $\mathbf{u}_{L,i}$  acts perpendicular to  $\mathbf{u}_{D,i}$  and in the longitudinal plane of the fluid dynamic surface.

The net moment acting about the center of mass of the kite is equal to the sum of moments caused by buoyancy, hydrodynamic lift and drag, and the tether tensions as follows:

$$\begin{aligned} \mathbf{M}_{\text{cm}} &= \mathbf{M}_B + \sum_{i=1}^4 \mathbf{M}_{L,i} + \sum_{i=1}^4 \mathbf{M}_{D,i} + \sum_{i=j}^3 \mathbf{M}_{T,j} \\ &= \mathbf{r}_b \times \mathbf{F}_B + \sum_{i=1}^4 \mathbf{r}_{a,i} \times (\mathbf{F}_{L,i} + \mathbf{F}_{D,i}) + \sum_{i=j}^{n_{\text{thr}}} \mathbf{r}_{\text{thr},j} \times \mathbf{F}_{\text{thr},j} \end{aligned} \quad (12)$$

Here,  $\mathbf{r}_{\text{thr},j}$  and  $\mathbf{r}_b$  are vectors going from the center of mass of the kite to the attachment point of the  $j$ th tether and the center of buoyancy, respectively.

**3.2 Tether Model.** The nominal tether design for the full-scale kite system involves a highly stiff structural Dyneema line, which contains a conductive element for signal transmission to/from the kite. In the lab-scale setup, a high-stiffness fishing line of appropriately scaled diameter is used to approximate tether behavior. In spite of its high stiffness, the tether can exhibit catenary geometry and elongations of around 1 percent under peak load, and is characterized as a chain of spring-damper elements and masses in order to appropriately capture these properties.

Specifically, we adopt a tether model used in Refs. [21] and [27], where the tethers are discretized into  $N_n$  nodes connected by  $(N_n - 1)$  cylindrical links modeled as massless noncompressive spring-dampers. Each node has six state variables which consist of its position  $\mathbf{r}_{i_n} \triangleq [x_{i_n} \ y_{i_n} \ z_{i_n}]^T$  and velocity  $\mathbf{v}_{i_n} \triangleq [\dot{x}_{i_n} \ \dot{y}_{i_n} \ \dot{z}_{i_n}]^T$  represented in the inertial frame, where  $i_n \in \{1, 2, \dots, N_n\}$ . The net force on any node is the sum of forces due to buoyancy, gravity, and fluid drag as follows:

$$\mathbf{F}_{i_n} = \mathbf{F}_{i_n}^b + \frac{\mathbf{F}_{i_n-1}^d + \mathbf{F}_{i_n}^d}{2} - \mathbf{F}_{i_n-1}^t + \mathbf{F}_{i_n}^t \quad (13)$$

Here,  $\mathbf{F}_{i_n}^b$  is the net buoyant force acting on node  $i_n$ ,  $\mathbf{F}_{i_n}^d$  is the fluid drag force acting on link  $i_n$ , and  $\mathbf{F}_{i_n}^t$  is the tensile force exerted by link  $i_n$ . The tensile force,  $\mathbf{F}_{i_n}^t$ , is zero if the link is unstretched and obeys Hooke's law if it is stretched. These forces are given by

$$\mathbf{F}_{i_n}^b = (\rho - \rho_T) \pi r_T^2 \frac{l_T}{N_n - 1} g \mathbf{k}_O \quad (14)$$

$$\mathbf{F}_{i_n}^d = C_{D,T} q_{i_n} A_{p,i_n} \frac{\mathbf{u}_{i_n}}{\|\mathbf{u}_{i_n}\|} \quad (15)$$

$$\mathbf{F}_{i_n}^t = \begin{cases} \mathbf{0} & \text{if } \|\mathbf{d}_{i_n}\| \leq \frac{l_T}{N_n - 1} \\ \left( \frac{E_T \pi r_T^2}{l_T (N_n - 1)} \left( \|\mathbf{d}_{i_n}\| - \frac{l_T}{N_n - 1} \right) + 2\zeta \sqrt{E_T \frac{\pi r_T^2}{l_T (N_n - 1)}} m \frac{d}{dt} \|\mathbf{d}_{i_n}\| \right) \frac{\mathbf{d}_{i_n}}{\|\mathbf{d}_{i_n}\|} & \text{otherwise} \end{cases} \quad (16)$$

where  $\rho_T$  is the tether density,  $r_T$  is the tether radius,  $l_T$  is the length of tether,  $E_T$  is the Young's modulus of the tether material, and  $\zeta$  is the damping ratio. The vector  $\mathbf{d}_{i_n}$  goes from node  $i_n$  to node  $(i_n + 1)$ . The switching condition in Eq. (16) checks for elastic deformation in the tether. If  $\|\mathbf{d}_{i_n}\| > l_T / (N_n - 1)$ , the deformation in link  $i_n$  is equal to  $(\|\mathbf{d}_{i_n}\| - l_T / (N_n - 1))$ . The terms  $q_{i_n}$ ,  $A_{p,i_n}$ , and  $\mathbf{u}_{i_n}$  represent the dynamic pressure, projected area, and the apparent flow for link  $i_n$ , respectively, and are calculated as follows:

$$\mathbf{u}_{i_n} = \mathbf{v}_f - \frac{\mathbf{v}_{i_n} + \mathbf{v}_{i_n+1}}{2} \quad (17)$$

$$q_{i_n} = \frac{1}{2} \rho \|\mathbf{u}_{i_n}\|^2 \quad (18)$$

$$A_{p,i_n} = 2r_T \frac{l_T}{N_n - 1} \left\| \frac{\mathbf{u}_{i_n}}{\|\mathbf{u}_{i_n}\|} \times \frac{\mathbf{d}_{i_n}}{\|\mathbf{d}_{i_n}\|} \right\| \quad (19)$$

The tether lengths are related to the tether spooling speed control inputs by

$$l_T = \int_0^t \text{sgn}(u_T) \min(\|u_T\|, u_{\text{max}}) dt \quad (20)$$

where  $u_{\max}$  is the maximum achievable tether spooling speed. The tether spooling impacts the tensile forces through the variation of the unstretched lengths of the tethers,  $l_T$ . When tether length is reduced (but node positions have not changed) through spool-in action, tension increases. In the opposite scenario, tension decreases.

#### 4 Control

In this section, we detail the control strategies used by the full-scale and the lab-scale systems. There are two general strategies for achieving cross-current motion:

1. *Path following*: This strategy involves first specifying and then following a spatially defined figure-8 path that is specifically designed to yield significant power production. Because power production is highly dependent on the azimuth and elevation angles of the kite, this strategy is generally the preferred approach for executing cross-current motion; however, its implementation not only requires low-latency real-time position estimates but also can only be reliably implemented with control over all three moments (roll, pitch, and yaw) at all times (which is accomplished with control surface actuation but not with tether actuation).

2. *Tether-based roll control*: This strategy involves specifying a time-based periodic roll setpoint trajectory for the kite to follow, then using asymmetric tether actuation (requiring multiple tethers or an actuated bridle) to induce roll motion. By rolling the kite, a lateral component of the kite's lift vector induces cross-current motion. Because the path is not explicitly defined, this strategy is generally not preferred; however, its implementation is simple and requires limited sensing and actuation.

The high sensing requirement and dependence on control surface actuation for path-following control prevent its implementation in the water channel environment. The dynamic model is therefore refined and validated by implementing the roll controller in the water channel and comparing the data against model predictions. However, the ultimate goal of the presented dynamic model is to simulate the dynamics of the full-scale system, which can operate under either a path-following controller or roll controller. Both control techniques are therefore described in Secs. 4.1 and 4.2 for completeness.

**4.1 Path-Following Controller.** The path-following controller is responsible for ensuring that the ocean kite tracks a prescribed figure-8 path, while spooling in at low tension and spooling out at high tension so as to produce positive net energy. This controller requires control surface actuation to achieve continuous control over the 3 moments acting about the center of mass of the body, in addition to a lot of space in the lateral direction for wide cross-current paths. Although this is a realistic possibility and indeed the most efficient way to operate in an open water environment, the same is not true for the water channel setup due to limitations on the size of the tank.

The controller adapts the modular hierarchical control structure presented in Ref. [28] for use with intracycle spooling, wherein spool-in and spool-out occur over different sections of the figure-

8, so as to maintain a constant mean depth of operation. The control structure, shown in Fig. 4, is partitioned into the following four blocks:

- (1) A *path-following* block, which accepts a path geometry and outputs a desired velocity angle;
- (2) A *tangent roll angle selection* block, which takes in the velocity angle and outputs a tangent roll angle;
- (3) A *desired moment selection* block, which accepts the tangent roll angle, and outputs a desired moment vector; and
- (4) A *control allocation* block, which takes in the desired moment vector to calculate the required control surface deflections.

**4.1.1 Path Following.** The path-following controller takes in the path defined by:

$$\Gamma(s) = \begin{Bmatrix} \cos(\lambda_\Gamma(s))\cos(\phi_\Gamma(s)) \\ \sin(\lambda_\Gamma(s))\cos(\phi_\Gamma(s)) \\ \sin(\lambda_\Gamma(s)) \end{Bmatrix} \quad (21)$$

where  $\Gamma(s)$  represents the path on a sphere in Cartesian coordinates, and  $\lambda_\Gamma(s)$  and  $\phi_\Gamma(s)$  are the longitudinal and latitudinal spherical coordinates that describe the kite's position along the path, given by the Lemniscate of Booth [28]. The variable  $s$  is a path parameter that varies from 0 to  $2\pi$ , describing the figure-8 path.

Given this path, we first calculate the path variable,  $s^*$ , corresponding to the closest point on the path, by numerically solving the following minimization problem:

$$s^* = \operatorname{argmin}_s \alpha(s), \quad \text{where} \quad \tan(\alpha(s)) = \frac{\|\mathbf{r}_{\text{cm}} \times \Gamma(s)\|}{|\mathbf{r}_{\text{cm}} \cdot \Gamma(s)|} \quad (22)$$

Here,  $\alpha(s)$  is the angle between the position vector,  $\mathbf{r}_{\text{cm}}$ , and the path  $\Gamma(s)$ . The closest path parameter,  $s^*$ , is used to calculate the perpendicular vector and the parallel vector. The perpendicular vector,  $\mathbf{p}_\perp^*$ , is the vector from the current position to the closest point on the path, while the parallel vector,  $\mathbf{p}_\parallel^*$ , is the vector tangent to the closest point

$$\mathbf{p}_\perp^* = \frac{\hat{p}_\perp}{\|\hat{p}_\perp\|}, \quad \text{where } \hat{p}_\perp = \begin{Bmatrix} (\Gamma(s^*) - \mathbf{r}_{\text{cm}}) \cdot \mathbf{j}_T(\mathbf{r}_{\text{cm}}) \\ (\Gamma(s^*) - \mathbf{r}_{\text{cm}}) \cdot \mathbf{k}_T(\mathbf{r}_{\text{cm}}) \\ 0 \end{Bmatrix} \quad (23)$$

$$\mathbf{p}_\parallel^* = \frac{\hat{p}_\text{allel}}{\|\hat{p}_\text{allel}\|}, \quad \text{where } \hat{p}_\text{allel} = \left. \frac{d\Gamma}{ds} \right|_{s=s^*} \quad (24)$$

The desired velocity unit vector is taken to be the average between the perpendicular vector and the parallel vector as follows:

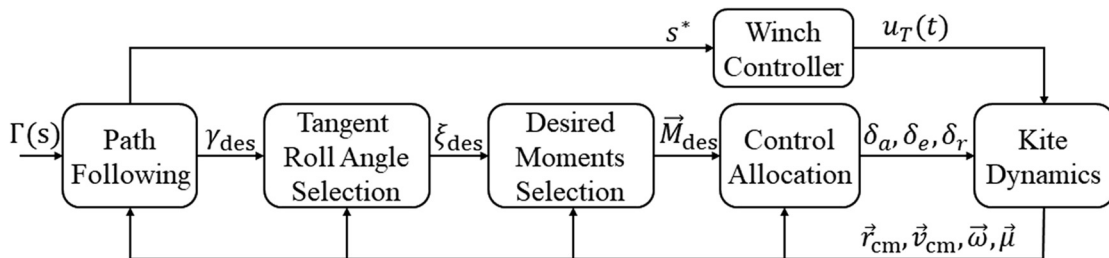


Fig. 4 Block diagram showing the hierarchical structure of the path-following controller

$$\begin{aligned}\bar{\alpha}(s^*) &= \min(\alpha(s^*), \alpha_0) \\ \mathbf{v}_{\text{des}} &= \left(1 - \frac{\bar{\alpha}(s^*)}{\alpha_0}\right) \mathbf{P}_{\text{allel}}^* + \frac{\bar{\alpha}(s^*)}{\alpha_0} \mathbf{P}_{\perp}^*\end{aligned}\quad (25)$$

Here,  $\alpha_0$  serves as an upper limit on the possible angle used in the weighting. Intuitively, it means that if the angle between the system and the path is more than  $\alpha_0$ , then the weighting will be entirely on the second term, making the system head directly toward the closest point on the path.

The velocity angle,  $\gamma$ , describes the orientation of the given velocity vector on the sphere of radius  $\|\mathbf{r}_{\text{cm}}\|$  at the current position,  $\mathbf{r}_{\text{cm}}$ , and is given by

$$\gamma(\mathbf{v}) = \arctan\left(\frac{\mathbf{v} \cdot \mathbf{i}_{\bar{T}}(\mathbf{r}_{\text{cm}})}{\mathbf{v} \cdot \mathbf{j}_{\bar{T}}(\mathbf{r}_{\text{cm}})}\right)\quad (26)$$

The desired velocity angle is then given by  $\gamma(\mathbf{v}_{\text{des}})$ .

**4.1.2 Tangent Roll Angle Selection.** The next stage of the controller maps the desired velocity angle to a desired tangent roll angle,  $\zeta_{\text{des}}$ . The tangent roll angle describes the orientation of the kite relative to the tangent plane and dictates the component of the hydrodynamic lift that contributes to turning. The tangent roll angle is calculated using a saturated proportional control based on the error in the velocity angle

$$\zeta_{\text{des}} = \min(\max(k_{\gamma}(\gamma(\mathbf{v}_{\text{cm}}) - \gamma(\mathbf{v}_{\text{des}})), \zeta_{\text{min}}), \zeta_{\text{max}})\quad (27)$$

where  $k_{\gamma}$  is the proportional gain. We then calculate an error signal,  $e_{\zeta}(t) = \zeta(\mathbf{j}_{\bar{B}}(t)) - \zeta_{\text{des}}$ , where the current tangent roll angle,  $\zeta(\mathbf{j}_{\bar{B}}(t))$ , is equal to the angle between the kite's  $\mathbf{j}_{\bar{B}}$  axis and the plane spanned by the unit vectors  $\mathbf{i}_{\bar{T}}$  and  $\mathbf{j}_{\bar{T}}$ , given by the following equation:

$$\tan(\zeta(\mathbf{j}_{\bar{B}}(t))) = \frac{\mathbf{j}_{\bar{B}} \cdot (\mathbf{j}_{\bar{T}} \times \mathbf{i}_{\bar{T}})}{\sqrt{(\mathbf{j}_{\bar{B}} \cdot \mathbf{i}_{\bar{T}})^2 + (\mathbf{j}_{\bar{B}} \cdot \mathbf{j}_{\bar{T}})^2}}\quad (28)$$

**4.1.3 Desired Moment Vector Selection.** In determining the desired moments, we utilize the rolling moment to control tangent roll angle,  $\zeta$ , and yawing moment to drive the hydrodynamic side slip angle,  $\beta$ , toward a value of zero. Because the tether spooling controller articulates the elevator to passively trim the system to a high angle of attack during spool-out and a low angle of attack during spool-in, it is desirable that the deflection of the ailerons and rudder contribute negligible or zero pitching moment. Ultimately, the desired moment vector is given by

$$\mathbf{M}_{\text{des}} = \begin{cases} k_{\text{pL}} e_{\zeta}(t) + k_{\text{iL}} \int_0^t e_{\zeta}(t) d\tau + k_{\text{dL}} \dot{e}_{\zeta}(t) \\ 0 \\ k_{\text{pN}} \beta + k_{\text{iN}} \int_0^t \beta d\tau + k_{\text{dN}} \dot{\beta} \end{cases}\quad (29)$$

**4.1.4 Control Allocation.** In order to map the desired moment vector to the control surface deflections, we invert a linearized approximation of the nonlinear mapping from deflections to hydrodynamic moments. This approximation is calculated by neglecting the effect of angular velocity on the apparent flow at each fluid dynamic surface, then linearizing to obtain an expression of the following form:

$$\mathbf{M}_{\text{net}} = \mathbf{M}_{\text{ext}} + A[\delta_{\text{a}} \quad \delta_{\text{e}} \quad \delta_{\text{r}}]^T\quad (30)$$

Here,  $\delta_{\text{a}}$ ,  $\delta_{\text{e}}$ , and  $\delta_{\text{r}}$  represent the deflections of the ailerons, elevator, and rudder, respectively.  $\mathbf{M}_{\text{ext}}$  is the sum of external moments given in Eq. (12), while the matrix  $A$  encodes the applied hydrodynamic moment due to control surface deflection and is given by

$$\begin{aligned}A &= \frac{1}{2} \rho A_{\text{r}} \|\mathbf{v}_{\text{f}} - \mathbf{v}_{\text{cm}}\|^2 [\mathbf{a}_1 - \mathbf{a}_2, \mathbf{a}_3, \mathbf{a}_4] \text{ where} \\ \mathbf{a}_i &= \mathbf{r}_{\mathbf{a}_i} \times \left( \frac{dC_{\text{L},i}}{d\delta_i} \mathbf{u}_{\text{L},i} + \frac{dC_{\text{D},i}}{d\delta_i} \mathbf{u}_{\text{D},i} \right)\end{aligned}\quad (31)$$

where  $(dC_{\text{L},i}/d\delta_i)$  and  $(dC_{\text{D},i}/d\delta_i)$  represent the change in the hydrodynamic lift and drag coefficients of the fluid dynamic surfaces per unit deflection of their respective control surfaces. The resulting control surface deflections are calculated by solving Eq. (30) for  $\mathbf{M}_{\text{net}} = \mathbf{M}_{\text{des}}$ , where  $\mathbf{M}_{\text{des}}$  is calculated in Eq. (29).

**4.2 Three Tether Controller.** The three tether controller is responsible for executing cross-current motion through the specification and subsequent tracking of a square wave roll angle setpoint through the actuation of three tethers. Although the cross-current motion achieved through this strategy is not as efficient as what is obtained from the path-following controller, this approach is more practical at lab scale, owing to fabrication limitations on the kite model that do not allow for active control surfaces, as well as size constraints on the water channel.

The tethers are attached on the port wing, starboard wing, and near the aft of the 3D printed model, as shown in Figs. 3, 5, and 6. Actuation of these three tethers enables direct control of three quantities:

- (1) Pitch,  $\theta$ , is controlled by spooling out the aft tether while spooling in the front tethers, or vice versa.
- (2) Roll,  $\phi$ , is controlled by spooling out the port tether and spooling in the starboard tether, or vice versa.
- (3) Altitude,  $z_{\text{cm}}$ , is controlled by spooling all tethers in or out simultaneously.

The goal of the kite's control system is to track a prescribed pitch angle setpoint ( $\theta_{\text{sp}}$ ), roll angle setpoint ( $\phi_{\text{sp}}$ ), and altitude setpoint ( $z_{\text{sp}}$ ) through the use of three separate controllers. Each of the three controllers, namely the altitude controller, pitch controller, and roll controller, is composed of a lead filter (i.e., a filtered proportional plus derivative controller). Because there exists a pure integrator between the controller commands and the tether lengths ( $l_{\text{T,port}}$ ,  $l_{\text{T,stbd}}$  and  $l_{\text{T,aft}}$ , which dictate  $\theta$ ,  $\phi$ , and  $z_{\text{cm}}$ ), an integrator is not included in the controller itself, as it is unnecessary for tracking sufficiently slowly varying commands and would lead to reduced stability margins if included. The control structure used in this work has been developed and utilized by the authors in Refs. [15], [18], [19], and [21], but is included in its entirety here for completeness. Figure 7 shows the block diagram of the control strategy.

The outputs from the three controllers are used to calculate the required actuation of each tether through linear combinations shown in Eqs. (32)–(34)

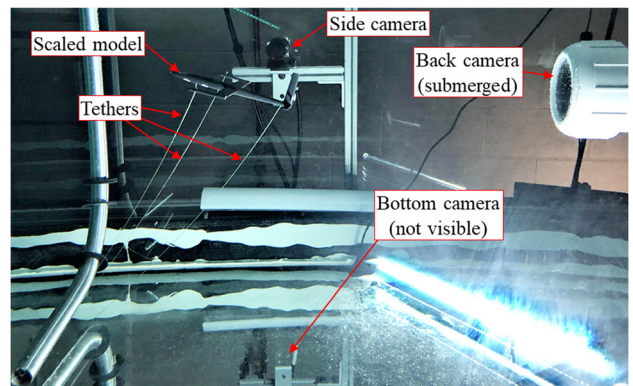
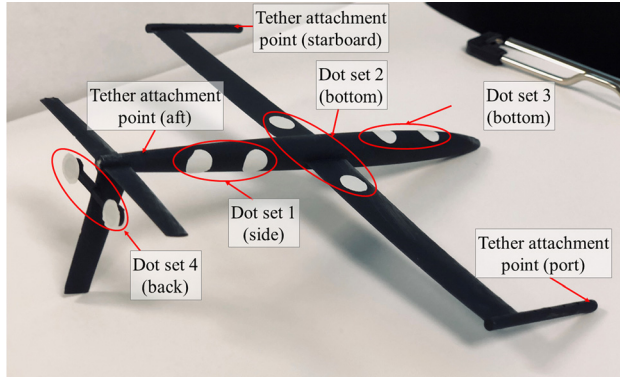
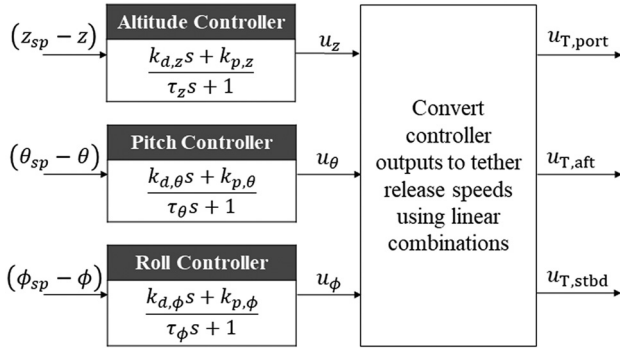


Fig. 5 Image of the experimental setup showing the scaled model, the side and the back cameras, and the tethers



**Fig. 6** Image of the 3D printed kite, showing the white dot sets as well as the tether attachment points



**Fig. 7** Block diagram of the three tether control strategy showing setpoints,  $z_{sp}$ ,  $\theta_{sp}$ , and  $\phi_{sp}$ ; and tether release commands,  $u_{T,port}$ ,  $u_{T,aft}$ , and  $u_{T,stbd}$

$$u_{T,port} = u_z + u_\theta + u_\phi \quad (32)$$

$$u_{T,aft} = u_z - u_\theta \quad (33)$$

$$u_{T,stbd} = u_z + u_\theta - u_\phi \quad (34)$$

To induce cross-current motion, the kite is commanded to follow a periodic roll angle profile. This results in a sideways component of the hydrodynamic lift vector, causing the kite to move laterally. One method to implement this strategy is to hold  $\theta_{sp}$  constant, while  $\phi_{sp}$  is varied periodically, according to a square wave profile given by

$$\phi_{sp}(t) = a_0 \operatorname{sgn} \left( \sin \left( \frac{2\pi}{T} t \right) \right) \quad (35)$$

where the wave amplitude ( $a_0$ ) and period ( $T$ ) represent tunable parameters that impact the quality of cross-current motion. The altitude controller is switched off prior to the initiation of cross-current operation.

## 5 Lab-Scale Measurement Setup

The purpose of the lab-scale experimental setup is to refine and validate the accuracy of the hydrodynamics, dynamics, and control model. In this setup, a 15/1000-scale model of the ocean kite is 3D printed, tethered, and “flown” in the water channel under controlled flow conditions. The kite is controlled via tether actuation, and motion is measured via a motion capture system. Controlled longitudinal (flow speed changes) and lateral (controlled asymmetric actuation of tethers) characteristics that can be reproduced in the dynamic model are defined and tested. The test setup is comprised of three main components:

- (1) The water channel, in which we “fly” the scaled model;
- (2) The 15/1000-scale model of the kite;
- (3) A motion capture system used to measure the position and orientation of the kite in real-time.

The lab-scale experiments were performed in North Carolina State University’s water channel, which has a test section that is 71.12 cm tall, 81.28 cm wide, 243.84 cm long, and can hold 13165.7 liters of water at full level. The freestream speed is controlled by 10 HP Baldor Reliance Super E Motor EM3774T that is connected to an ABB ACS355 (ABB Motors and Mechanical Inc., Fort Smith, AR) variable frequency drive and is capable of generating flow speeds from 0.16 m/s to 1 m/s. At a flow speed of 0.166 m/s, the turbulence intensity for the streamwise component of flow velocity at a height of 31.1 cm was estimated at 0.20%, and the flow nonuniformity over the entire test section was estimated to be 1% [29].

A 3D printed model of the ocean kite, whose cross-sectional area comprises less than 1.5% of the total water channel cross-sectional area, is tethered and “flown” in the water channel, as shown in Fig. 5. Due to size constraints, it is infeasible to mount an IMU on the scaled model for position and orientation measurement. Therefore, these quantities were measured using a motion capture system detailed in Ref. [20].

The experimental equipment consists of three DC motors for tether actuation, three high-speed cameras for image acquisition, and a high-performance host/target computer pair for real-time motion capture and closed-loop control. Four SPEEDGOATS (real-time target computers designed to work with SIMULINK real-time), three for image processing and one for real-time control, are used for fast computation. The system uses three Basler ACE 340 km grayscale cameras to obtain real-time images of the model. The use of three mutually perpendicular cameras provides sufficient image data to resolve the position ( $x_{cm}$ ,  $y_{cm}$ , and  $z_{cm}$ ) and orientation ( $\phi$ ,  $\theta$ ,  $\psi$ ) of the model. A schematic diagram of the experimental setup is shown in Fig. 3.

**5.1 Motion Capture System.** The position and orientation of the kite are estimated by tracking the white dots on the model shown in Fig. 6. Thus, in order to successfully execute closed-loop cross-current motion, the motion capture system must be able to track these dots accurately and continuously. This subsection provides an overview of the motion capture system used to achieve this goal, which is described in detail in Ref. [20].

**5.1.1 Dot Centroid Location.** The first step in resolving the position and orientation of the kite is to locate the white dots in the three images. We do this by first extracting a small region of interest (ROI) from the image of each camera. This is followed by classifying each pixel in the ROI as either belonging to a dot or background, using a grayscale thresholding technique called Otsu’s method [30]. The outputs of the image processing block are the pixel locations of the eight white dots belonging to the four dot sets.

**5.1.2 Euler Angles and Position Calculation.** Each set of dots is aligned with either the body-fixed  $x$ - or  $y$ -axis; specifically, two of the ROIs track dots oriented along the  $\mathbf{i}_{\bar{B}}$  axis, whereas the other two track dots that are oriented along the  $\mathbf{j}_{\bar{B}}$  axis. Table 1

**Table 1** Resolution of specific body-fixed axes components

Unit vector	Component	Camera	Dot set
$\mathbf{i}_{\bar{B}}$	$x_{cm}$	Side	1
$\mathbf{i}_{\bar{B}}$	$y_{cm}$	Bottom	3
$\mathbf{i}_{\bar{B}}$	$z_{cm}$	Side	1
$\mathbf{j}_{\bar{B}}$	$x_{cm}$	Bottom	2
$\mathbf{j}_{\bar{B}}$	$y_{cm}$	Bottom	2
$\mathbf{j}_{\bar{B}}$	$z_{cm}$	Back	4

**Table 2 List of experimental flow speeds and controller parameters**

Run	$\ \mathbf{v}_f\ $ (m/s)	Pitch				Roll				
		$\theta_{sp}$ (deg)	$k_{p,\theta}$ (m/rad-s)	$k_{d,\theta}$ (m/rad)	$\tau_\theta$ (s)	$a_0$ (deg)	$T$ (s)	$k_{p,\phi}$ (m/rad-s)	$k_{d,\phi}$ (m/rad)	$\tau_\phi$ (s)
1	0.245	14	1	2	0.3	12	6	2	4	0.5
2	0.262	14	1	2	0.3	13	6	2	4	0.5
3	0.279	14	1	2	0.3	13	5.5	2.25	4.5	0.5
4	0.296	14	1	2	0.3	13	5.5	2.25	4.5	0.5
5	0.313	14	1	2	0.3	13	5	2.5	5	0.5
6	0.330	14	1	2	0.3	13	5	2.5	5	0.5
7	0.347	14	1	2	0.3	13	4.75	2.5	5	0.5
8	0.364	14	1	2	0.3	13	4.75	2.5	5.5	0.5
9	0.381	14	1	2	0.3	13	4.75	2.75	5.5	0.5
10	0.381	14	1	2	0.3	14	4.75	2.75	5.5	0.5
11	0.390	14	1	2	0.3	14	4.75	3	5.5	0.5
12	0.398	14	1	2	0.3	14	4.5	3	5.5	0.5

Note: The values of  $a_0$  and  $T$  were chosen to obtain appreciable motion in the lateral direction while ensuring that the tracking dots remained in the field of view of all cameras.

delineates the geometric information that is provided by each camera and each set of dots. This information is sufficient for the calculation of the unit vectors  $\mathbf{i}_{\bar{B}}$  and  $\mathbf{j}_{\bar{B}}$  in the inertial frame. Once  $\mathbf{i}_{\bar{B}}$  and  $\mathbf{j}_{\bar{B}}$  have been determined,  $\mathbf{k}_{\bar{B}}$  is determined from a simple cross-product; specifically,  $\mathbf{k}_{\bar{B}} = \mathbf{i}_{\bar{B}} \times \mathbf{j}_{\bar{B}}$ . The complete set of body-fixed unit vectors in the inertial frame forms the columns of a rotation matrix that encodes the Euler angles, namely roll ( $\phi$ ), pitch ( $\theta$ ), and yaw ( $\psi$ ).

As the position of the model is necessary to determine the conversion factor between pixels and distance, and because position is required for dynamic characterization and motion control,  $\mathbf{r}_{cm}$  is also computed at each time-step. This is accomplished by using the dot centroid position of each set of dots and the Euler angles to calculate a least squares fit for the position of the center of mass of the kite.

## 6 Dynamic Model Refinement and Validation

The lab-scale experimental data collected were used to refine and validate the dynamic model presented in Sec. 3. The refinement and validation process can be summarized in three steps:

- (1) Collect experimental data over a range of flow speeds and variations in controller parameters;
- (2) Refine the model to fit a small set of experimental data; and
- (3) Validate the refined model against a larger set of experimental data.

**6.1 Collection of Experimental Data.** The scaled model was subjected to the three tether cross-current motion control algorithm described in Sec. 4 at various flow speeds, for a duration of at least 30 periods of the square wave roll setpoint (Eq. (35)), amounting to between 135 s and 180 s of data. Table 2 provides a list of the flow and controller parameters that were used in the experimental runs.

The collected datasets were split into two groups: one group for model refinement and another for validation. The refinement datasets were used to identify and refine the values of critical simulation parameters, whereas the validation datasets were used to test the quality of fit of the refined parameters.

**6.2 Model Refinement.** The dynamic model presented in Sec. 3 is driven by a large number of simulation parameters. The system parameters that can be directly measured, obtained from the computer-aided design or data sheets, are listed in Table 3. On the other hand, to accurately measure hydrodynamic parameters like the lift and drag coefficients of the fluid dynamic surfaces ( $C_{L,i}$ ,  $C_{D,i}$ ), and the added mass ( $m_{a,x}$ ,  $m_{a,y}$ ,  $m_{a,z}$ ), elaborate experimental setups and several person-hours worth of experiments are

**Table 3 Important system parameters at lab scale**

Variable	Description	Value	Unit
Kite			
$m$	Mass	9.55	g
$V$	Volume	10.24	cm <sup>3</sup>
$I_{xx}$	Inertia tensor $xx$ element	83.1	g cm <sup>2</sup>
$I_{yy}$	Inertia tensor $yy$ element	94.7	g cm <sup>2</sup>
$I_{zz}$	Inertia tensor $zz$ element	174.2	g cm <sup>2</sup>
$A_r$	Reference area	22.5	cm <sup>2</sup>
$b_w$	Wing span	15	cm
$c_w$	Wing chord	1.5	cm
$t_w$	Wing thickness	0.14	cm
$b_{hs}$	Horizontal stabilizer span	6	cm
$c_{hs}$	Horizontal stabilizer chord	0.75	cm
$t_{hs}$	Horizontal stabilizer thickness	0.09	cm
$b_{vs}$	Vertical stabilizer span	3.6	cm
$c_{vs}$	Vertical stabilizer chord	0.9	cm
$t_{vs}$	Vertical stabilizer thickness	0.11	cm
Tethers			
$r_T$	Radius	0.15	mm
$\rho_T$	Density	1300	kg/m <sup>3</sup>
$E_T$	Young's modulus	0.4	GPa
$\zeta$	Damping ratio	0.02	–
$C_{D,T}$	Drag coefficient	0.5	–

required. Steady-state estimates of these parameters are more readily available through the use of computational software [26] and empirical relations [25], and are listed in Table 4. But owing to the dynamic nature of the system, these steady-state estimates are most susceptible to inaccurate characterization and are therefore chosen as the candidate parameters that need to be refined.

In this work, we correct the initial estimates of the uncertain parameters by multiplying them by numerically optimized scaling coefficients. These coefficients are optimized by minimizing an objective function that is equal to the weighted sum of root-mean-squared errors (RMSE) between the simulated and measured values of the roll angle ( $\phi$ ), yaw angle ( $\psi$ ), and  $y$ -position ( $y_{cm}$ ).

**Table 4 Uncertain parameters, their initial values, and corresponding scaling coefficients at lab scale**

Variable	Description	Initial estimate	Unit	Scaling coefficients
$m_{a,x}$	Added mass in $\mathbf{i}_{\bar{B}}$	0.28	g	$c_1$
$m_{a,y}$	Added mass in $\mathbf{j}_{\bar{B}}$	2.71	g	$c_2$
$m_{a,z}$	Added mass in $\mathbf{k}_{\bar{B}}$	23.75	g	$c_3$
$C_{L,i}$	Lift coefficients	Fig. 11	–	$c_4, c_5, c_6$
$C_{D,i}$	Drag coefficients	Fig. 11	–	$c_7, c_8, c_9$

Table 4 lists the uncertain parameters, their initial estimates, and corresponding scaling coefficients. The optimization problem is formulated as follows:

$$\begin{aligned}
c_i^* &= \operatorname{argmin}_{c_i} (w_1 R_\phi + w_2 R_\psi + w_3 R_y) \\
&= \operatorname{argmin}_{c_i} \left( w_1 \sqrt{\frac{\sum_{i=1}^n (\phi_{\text{exp},i} - \phi_{\text{sim},i})^2}{n}} \right. \\
&\quad \left. + w_2 \sqrt{\frac{\sum_{i=1}^n (\psi_{\text{exp},i} - \psi_{\text{sim},i})^2}{n}} + w_3 \sqrt{\frac{\sum_{i=1}^n (y_{\text{exp},i} - y_{\text{sim},i})^2}{n}} \right) \\
\text{Subject to: } & 0.5 \leq c_j \leq 1.5 \quad \text{for } j = 1, 2, \dots, 9
\end{aligned} \tag{36}$$

Here,  $R_\phi$ ,  $R_\psi$ , and  $R_y$  are RMSE in roll angle, yaw angle, and  $y$ -position, respectively;  $\phi_{\text{exp},i}$ ,  $\psi_{\text{exp},i}$ , and  $y_{\text{exp},i}$  are the experimentally measured values of the roll angle, yaw angle, and  $y$ -position of the kite at time-step  $i$ .  $n$  is the total number of time-steps over a course of the experiment ( $n = 6000$  for a 60 s experiment). The constraints on the scaling coefficients were imposed to allow for  $\pm 50\%$  error in the initial estimate of the uncertain parameters. Optimized values of  $c_i$  close to 1 would indicate a good initial characterization of the uncertain parameter associated with the scaling coefficient.

Given the fact that the optimization of  $c_i$  values amounts to a complex, nonconvex optimization (owing to the complex and highly nonlinear nature of the dynamic model), we pursue a two-step optimization technique that consists of both a global search and local refinement. Specifically, the optimization problem is broken into two steps:

- (1) Perform a coarse optimization using particle swarm optimization (PSO) to locate the region containing the global minimum;
- (2) Refine the result by feeding the PSO result as an initial guess to a lower-level local optimizer.

*Particle swarm optimization* is a population-based stochastic search algorithm first introduced by Kennedy and Eberhart [31]. The algorithm attempts to mimic the natural process of group communication in swarms of birds, insects, etc. In PSO, each member of the swarm is modeled as a particle with certain position and velocity in an objective function space. Starting with a randomly initialized population, each particle explores the objective function space and remembers the best position it has seen. Members of a swarm communicate good positions with each other and iteratively adjust their own positions and velocities based on these good positions. The velocity adjustment is based upon the historical behaviors of the particles themselves as well as the entire swarm. The exploration procedure based on this concept can be described by

$$v_i^{k+1} = v_i^k + c_1 R_1 (p_{\text{best},i} - x_i^k) + c_2 R_2 (g_{\text{best}} - x_i^k) \tag{37}$$

$$x_i^{k+1} = x_i^k + v_i^{k+1} \tag{38}$$

where  $c_1$  and  $c_2$  are positive constants, known as the cognitive and social learning rates, respectively;  $R_1$  and  $R_2$  are two uniformly distributed random numbers between 0 and 1;  $x_i$  is the position of the  $i$ th particle and  $p_{\text{best},i}$  represents its best previous position;  $g_{\text{best}}$  is the best position in the entire population;  $v_i$  is the rate of position change for particle  $x_i$ . Every particle's current position is evolved according to Eq. (38). The implementation of the PSO algorithm is illustrated in the flowchart shown in Fig. 8.

The results from the PSO are used as the initial guess given to a local optimization algorithm. The advantage of these algorithms is that they are very efficient at converging quickly on local optima. Sequential quadratic programming was adopted for this purpose.

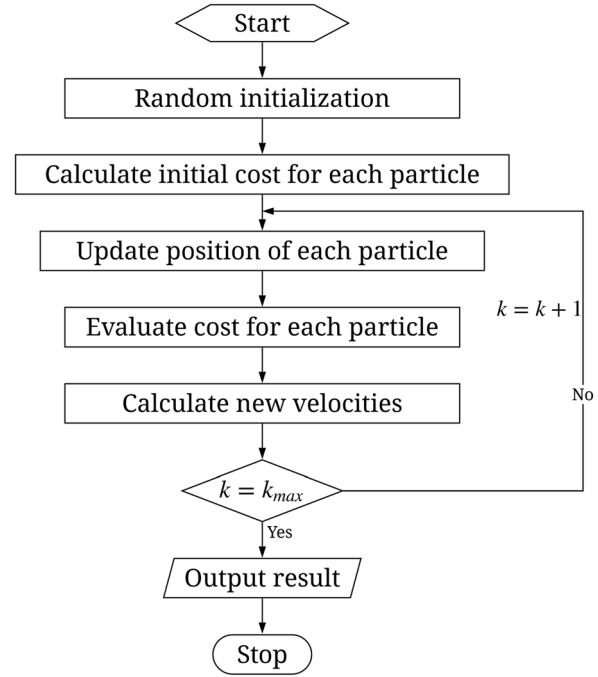


Fig. 8 Flowchart for PSO algorithm

Briefly, the sequential quadratic programming algorithm determines the optimum by solving a sequence of optimization subproblems, each of which optimizes a quadratic approximation of the objective function subject to a linearization of the constraints.

**6.3 Validation.** The purpose of validation is to demonstrate that the best fit scaling coefficients are not unique to one particular experimental run. We do this by using the refined uncertain parameters to run simulations and comparing the results with the validation group of experimental datasets.

The quality of fit between the predicted and measured values is quantified by calculating the RMSE values described by  $R_\phi$ ,  $R_\psi$ , and  $R_y$ , along with “aggregate” metrics that quantify the differences in amplitude and phase shift between the experimental validation data and model predictions. The equations for these additional “aggregate” metrics are as follows:

$$A_\phi = \frac{\sqrt{\frac{\sum_{i=1}^{n_p} \phi_{\text{sim},i}^2}{n_p}} - \sqrt{\frac{\sum_{i=1}^{n_p} \phi_{\text{exp},i}^2}{n_p}}}{\max(\phi_{\text{exp}}) - \min(\phi_{\text{exp}})} \tag{39}$$

$$A_\psi = \frac{\sqrt{\frac{\sum_{i=1}^{n_p} \psi_{\text{sim},i}^2}{n_p}} - \sqrt{\frac{\sum_{i=1}^{n_p} \psi_{\text{exp},i}^2}{n_p}}}{\max(\psi_{\text{exp}}) - \min(\psi_{\text{exp}})} \tag{40}$$

$$A_y = \frac{\sqrt{\frac{\sum_{i=1}^{n_p} y_{\text{sim},i}^2}{n_p}} - \sqrt{\frac{\sum_{i=1}^{n_p} y_{\text{exp},i}^2}{n_p}}}{\max(y_{\text{exp}}) - \min(y_{\text{exp}})} \tag{41}$$

$$P_\phi = \frac{2}{T} \frac{\sum_{i=1}^{n_z-1} (t_{\text{sim},i+1}^\phi - t_{\text{sim},i}^\phi) - \sum_{i=1}^{n_z-1} (t_{\text{exp},i+1}^\phi - t_{\text{exp},i}^\phi)}{n_z - 1} \tag{42}$$

$$P_\psi = \frac{2}{T} \frac{\sum_{i=1}^{n_z-1} (t_{\text{sim},i+1}^\psi - t_{\text{sim},i}^\psi) - \sum_{i=1}^{n_z-1} (t_{\text{exp},i+1}^\psi - t_{\text{exp},i}^\psi)}{n_z - 1} \tag{43}$$

**Table 5 Scaling coefficient optimization results**

Variable	Description	Scaling coefficient	Value
$m_{a,x}$	Added mass in $\mathbf{j}_{\bar{B}}$	$c_1$	0.543
$m_{a,y}$	Added mass in $\mathbf{j}_{\bar{B}}$	$c_2$	1.135
$m_{a,z}$	Added mass in $\mathbf{k}_{\bar{B}}$	$c_3$	0.782
$C_{L,w}$	Half wing lift coefficient	$c_4$	0.989
$C_{L,hs}$	Horizontal stabilizer lift coefficient	$c_5$	0.961
$C_{L,vs}$	Vertical stabilizer lift coefficient	$c_6$	0.992
$C_{D,w}$	Half wing drag coefficient	$c_7$	1.096
$C_{D,hs}$	Horizontal stabilizer drag coefficient	$c_8$	1.103
$C_{D,vs}$	Vertical stabilizer drag coefficient	$c_9$	1.095

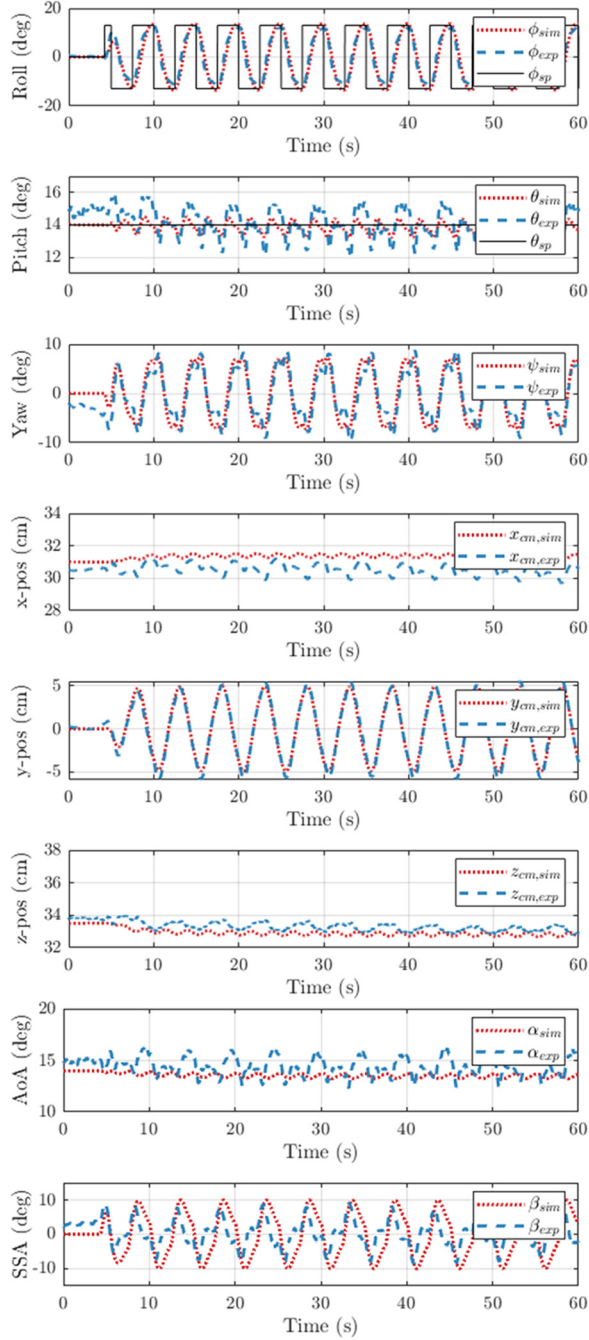


**Fig. 9 Postrefinement results for run 6 showing the simulation versus experimental plots for Euler angles, center of mass position, angle of attack, and side-slip angle**

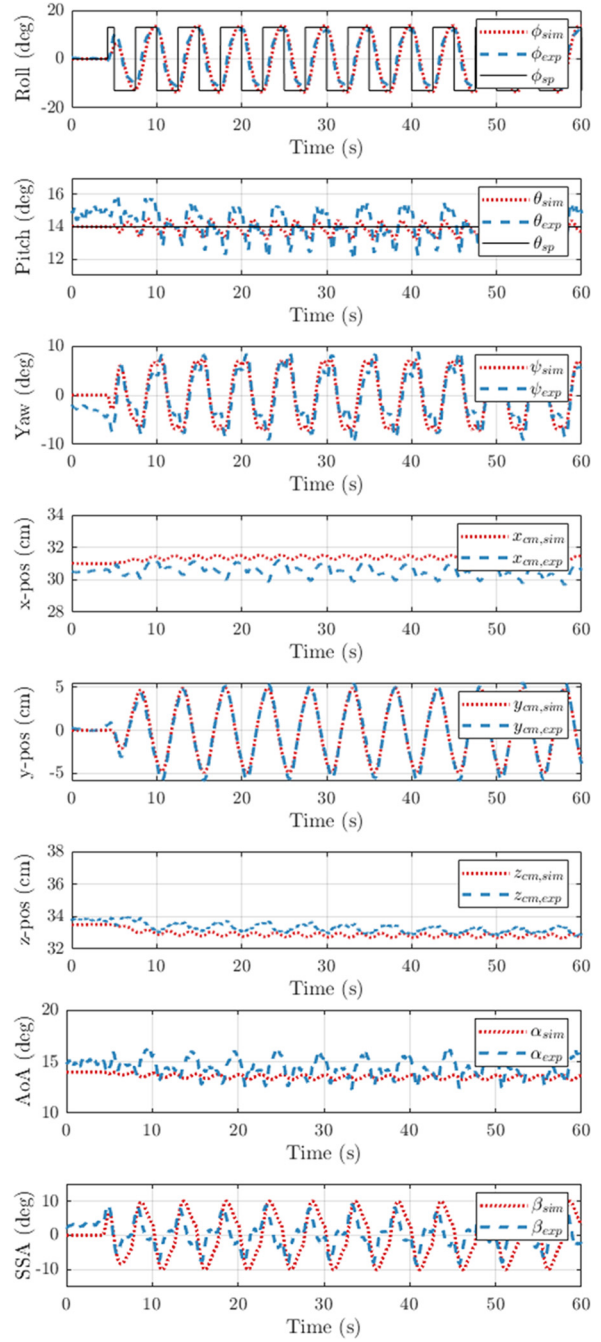


**Fig. 10 Postrefinement results for run 7 showing the simulation versus experimental plots for Euler angles, center of mass position, angle of attack, and side-slip angle**

$$P_y = \frac{2}{T} \frac{\sum_{i=1}^{n_z-1} (t_{\text{sim},i+1}^y - t_{\text{sim},i}^y) - \sum_{i=1}^{n_z-1} (t_{\text{exp},i+1}^y - t_{\text{exp},i}^y)}{n_z - 1} \quad (44)$$

Here,  $n_p$  and  $n_z$  are number of peaks and number of zero-crossings during the duration of the experiment, respectively.  $A_\phi$ ,  $A_\psi$ , and  $A_y$  are the differences between the average amplitude of the roll angle, yaw angle, and the  $y$ -position, respectively;  $P_\phi$ ,  $P_\psi$ , and  $P_y$  are the differences between the average periods of the roll angle, yaw angle, and the  $y$ -position, respectively.

**Table 6 Validation results listing the values of average amplitudes, average periods, and RMSE in the roll angle, yaw angle, and y-position**

Run	$A_\phi$ (%)	$A_\psi$ (%)	$A_y$ (%)	$P_\phi$ (%)	$P_\psi$ (%)	$P_y$ (%)	$R_\phi$ (deg)	$R_\psi$ (deg)	$R_y$ (cm)
2	10.43	6.86	14.48	0.03	0.07	0.12	2.32	4.24	1.20
4	3.89	2.44	8.07	0.05	0.14	0.09	1.77	4.07	0.78
6	2.63	2.36	3.24	0.04	0.03	0.03	1.66	4.05	0.39
8	6.05	6.16	3.90	0.01	0.06	0.01	3.17	2.86	0.54
10	7.64	9.45	3.23	0.02	0.03	0.04	3.95	2.28	0.88
12	7.53	6.86	3.88	0.04	0.08	0.12	4.95	1.64	1.34

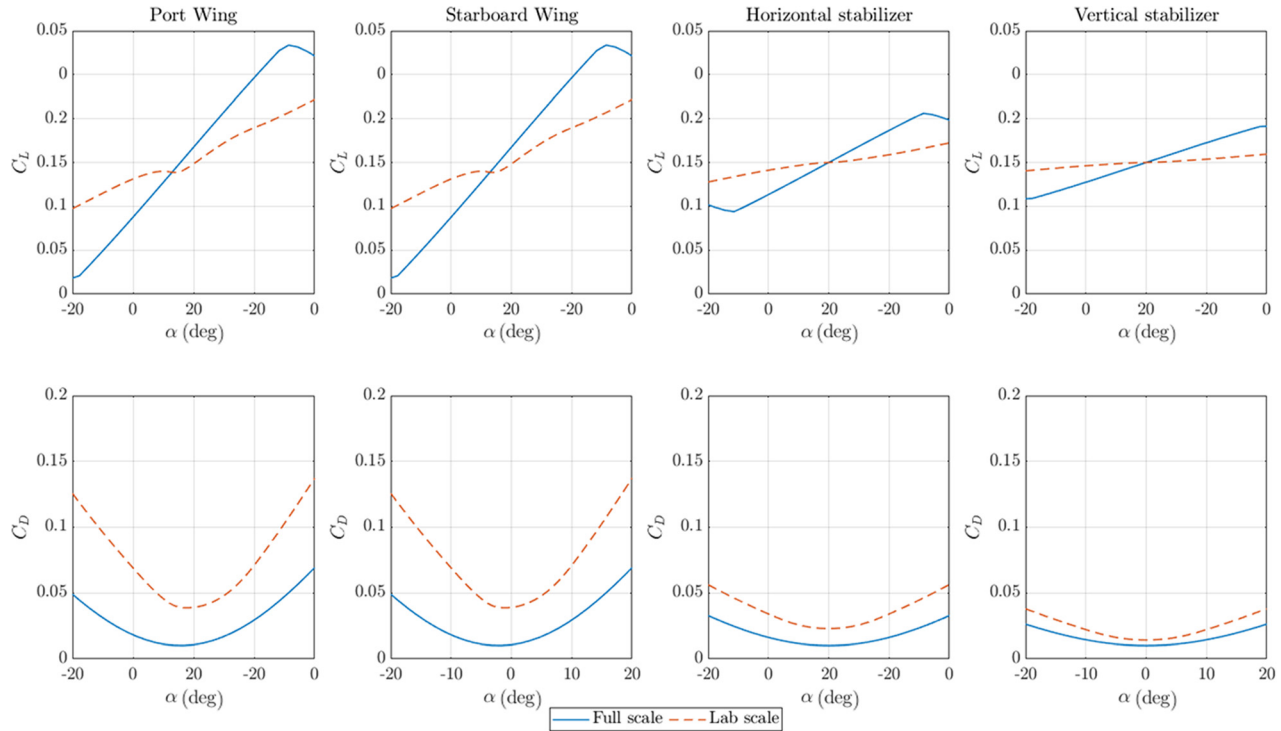


**Fig. 11  $C_L$  and  $C_D$  curves for fluid dynamic surfaces of the lab-scale and full-scale kite calculated using the wing planform area as reference area**

## 7 Refinement Results

The mathematical model was simulated using SIMULINK, via an ode23 stiff differential equation solver with a maximum time-step of 0.1s. Since the sampling frequency of the experiment was 100 Hz, the simulation results were resampled at the same frequency to allow direct comparison. The scaling coefficients were then optimized using the formulation shown in Eq. (37). The weighting terms ( $w_1, w_2, w_3$ ) on the RMSE values of the roll angle, yaw angle, and y-position were set to 1, 1, and 5, respectively. The numerical optimization was performed for different datasets to test for uniqueness of solution over a range of conditions. The resulting optimized scaling coefficients are listed in Table 5.

The accuracy of the dynamic model postrefinement was demonstrated by using the optimized scaling coefficients and comparing simulation results against a different set of experiments. Figures 9 and 10 show simulation versus experimental plots for the Euler angles and center of mass positions obtained after numerical optimization of the scaling coefficients. The results of model validation using the performance metrics listed in Eqs. (39)–(44), as well as the RMSE values defined in Eq. (37) are summarized in Table 6.

It is worth noting that the refinement and validation is being done with closed-loop control in place. However, the only states

**Table 7 Important system parameters at full scale**

Variable	Description	Value	Unit
<b>Kite</b>			
$m$	Mass	2917	kg
$V$	Volume	3.033	$m^3$
$I_{xx}$	Inertia tensor $xx$ element	10941	$kg \cdot m^2$
$I_{yy}$	Inertia tensor $yy$ element	12476	$kg \cdot m^2$
$I_{zz}$	Inertia tensor $zz$ element	24676	$kg \cdot m^2$
$A_r$	Reference area	10	$m^2$
$b_w$	Wing span	10	m
$c_w$	Wing chord	1	m
$t_w$	Wing thickness	0.1	m
$b_{hs}$	Horizontal stabilizer span	4	m
$c_{hs}$	Horizontal stabilizer chord	0.45	m
$t_{hs}$	Horizontal stabilizer thickness	0.06	m
$b_{vs}$	Vertical stabilizer span	2.44	m
$c_{vs}$	Vertical stabilizer chord	0.59	m
$t_{vs}$	Vertical stabilizer thickness	0.07	m
<b>Tethers</b>			
$r_T$	Radius	0.01	m
$\rho_T$	Density	1300	$kg/m^3$
$E_T$	Young's modulus	26.67	GPa
$\zeta$	Damping ratio	0.02	–
$C_{D,T}$	Drag coefficient	0.5	–

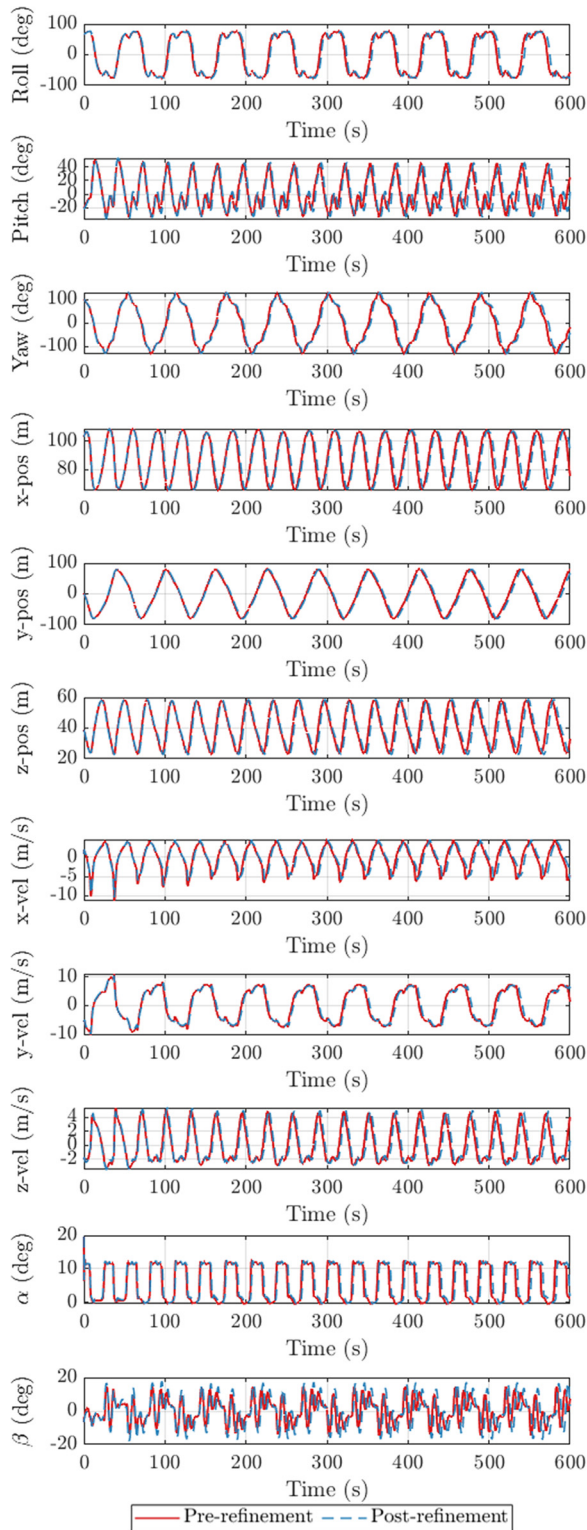


**Fig. 12** Full-scale simulation results for kite executing cross-current motion using the path-following controller before and after using the optimized scaling coefficients

that are controlled to setpoints are the pitch angle and the roll angle, whereas the quality of fit is quantified by calculating errors in the roll angle, yaw angle, and y position, the latter two being uncontrolled states. Close agreement is further observed in the  $x$  and  $z$  positions (visible in Figs. 9 and 10), neither of which are controlled in the experiments (while the  $z$  position is controlled

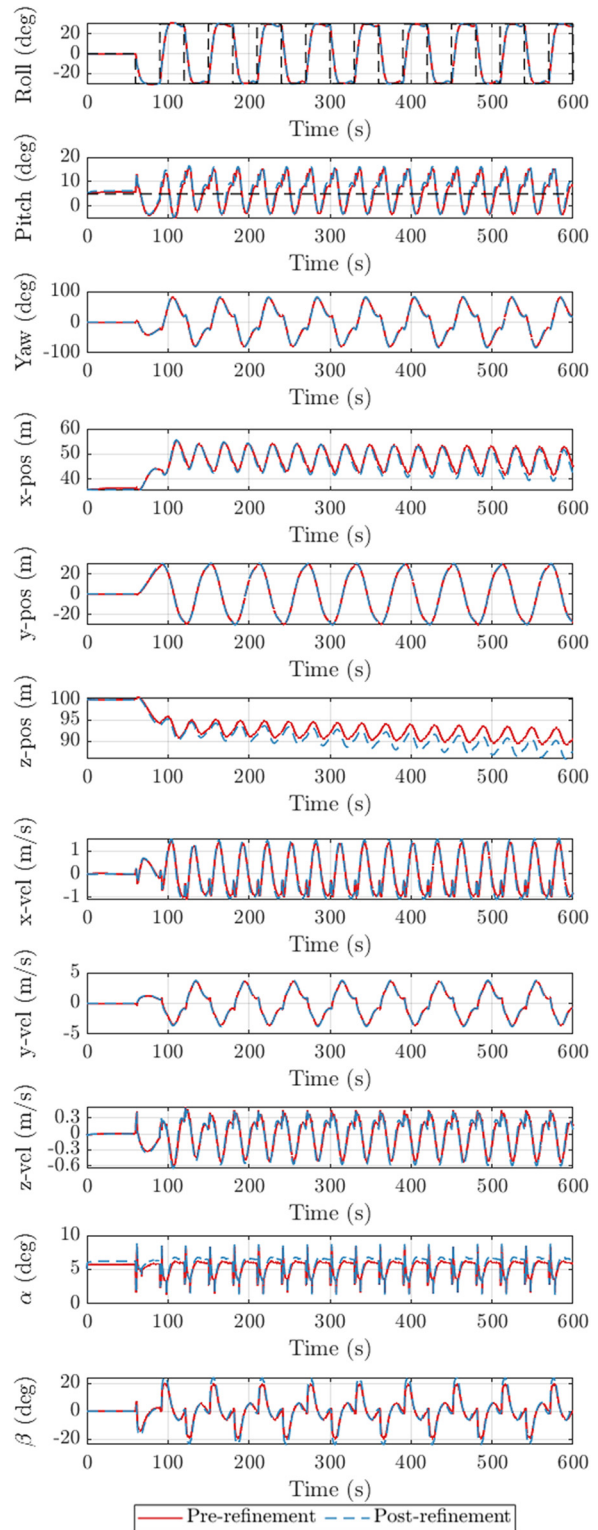


**Fig. 13** Full-scale simulation results for kite executing cross-current motion using the three tether controller before and after using the optimized scaling coefficients

prior to the initiation of cross-current motion, altitude control is suspended during cross-current motion).

## 8 Extrapolation to Full Scale

To evaluate the performance of the lab-scale kite design extrapolated to full scale, we simulated the full-scale system in a

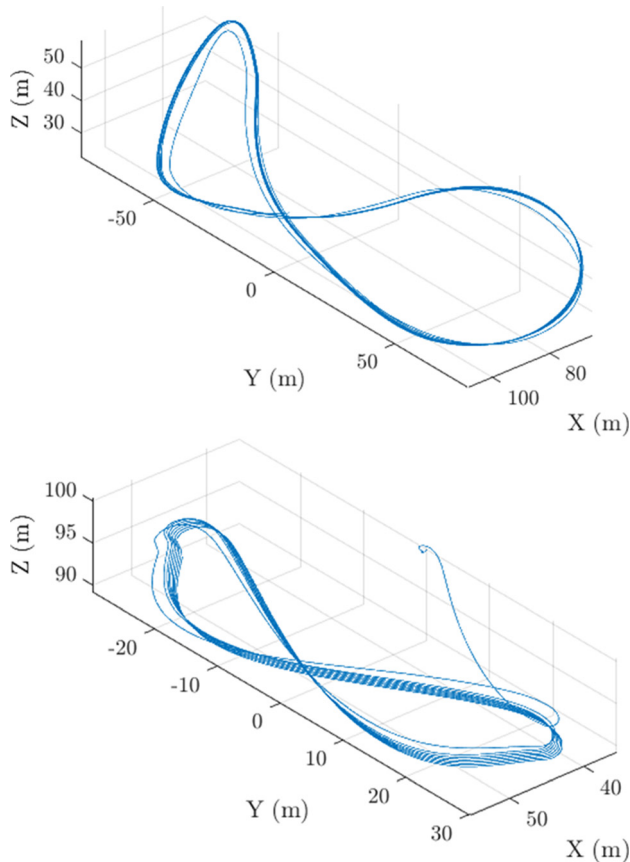


**Fig. 14** Paths traced by the kite using the path-following controller (top) and the three tether controller (bottom) while executing cross-current motion

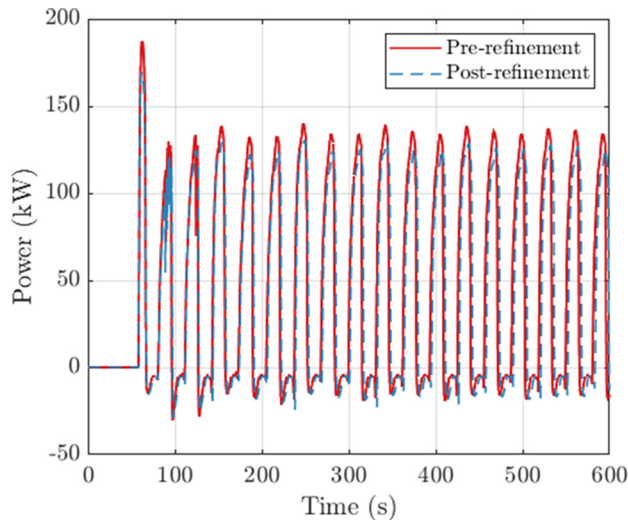


**Fig. 15** Power generated at full scale using the path-following controller

constant flow speed of 2 m/s. The lab-scale system design parameters were scaled to full scale through the following scaling laws:

- (1) The units of length were scaled by the geometric scale factor;
- (2) The units of mass were scaled by the cube of the geometric scale factor; and
- (3) The units of time (which appear in control parameters) were scaled by the square root of the geometric scale factor.

Each of these scaling rules follows the dynamic equivalence results derived using dimensional analysis in Refs. [18] and [20]. Owing to Reynolds number differences ( $Re \approx 10^4$  at lab scale,  $Re \approx 10^6$  at full scale), hydrodynamic coefficients will differ at lab- and full-scale, as seen in Fig. 11. Consequently, extrapolation to full-scale operation requires identification of the appropriate (revised) hydrodynamic coefficients at full scale. The kite parameters, when scaled up to full scale using these guidelines, are detailed in Table 7.

**8.1 Simulation Results.** For the purposes of completeness and to contrast the performance of the two controllers, we present simulation results for a full-scale system executing cross-current motion using both the path-following controller as well as the three tether controller, as shown in Figs. 12 and 13, respectively. Figure 14 shows the paths traced by the kite when using the two controllers. A plot of instantaneous power generated during control surface-actuated operation is shown in Fig. 15. The mean tether length for both simulations is approximately 110 m, and the roll amplitude for the three tether simulation in 30 deg. Note that the full-scale quality of cross-current motion, evident from the range of motion and velocity in the lateral direction, exhibited through the implementation of the path-following controller, is far better than what is achieved by using the three tether controller. This is because the path-following controller uses control surface deflection to continually control the elevation angle,  $\phi_T$ , which directly impacts the quality of cross-current motion, as shown by Ref. [7].

Figures 12 and 13 also show simulation results before and after the use of numerically optimized scaling coefficients, which demonstrates that the full-scale model is relatively insensitive to small changes in the candidate parameters that were numerically refined. Given that the correction coefficients identified in the refinement are not guaranteed to extrapolate to full scale, this relative insensitivity represents a strong indication that the dynamic model, which has been shown to be accurate at lab scale, will indeed compare favorably with full-scale experiments.

## 9 Conclusion

In this work, we presented a generalized dynamic model for a marine hydrokinetic kite, followed by a method to experimentally characterize the closed-loop dynamics of a lab-scale prototype. We then presented a method to refine the dynamic model through parameter identification and numerical optimization. The refined model of the system was then extrapolated to full scale, and the corresponding closed-loop dynamics were characterized.

Future work will involve physics-based characterizations of unsteady flow effects in the water channel, along with extrapolation of these characterizations to full-scale operation.

## Funding Data

- U.S. Department of Energy (Award No. DE-EE0008635; Funder ID: 10.13039/100000015).

## References

- [1] Archer, C. L., and Caldeira, K., 2008, "Atlas of High Altitude Wind Power," *Carnegie Institute for Science*, Washington, DC.
- [2] Moodley, R., Nthontho, M., Chowdhury, S., and Chowdhury, S., 2012, "A Technical and Economic Analysis of Energy Extraction From the Agulhas Current on the East Coast of South Africa," *IEEE Power and Energy Society General Meeting*, San Diego, CA, July 22–26, pp. 1–8.
- [3] Duerr, A. E., and Dhanak, M. R., 2012, "An Assessment of the Hydrokinetic Energy Resource of the Florida Current," *IEEE J. Oceanic Eng.*, **37**(2), pp. 281–293.
- [4] Landberg, M., 2012, "Submersible Plant," U.S. Patent No. 8,246,293.
- [5] Coiro, D., Troise, G., Scherillo, F., De Marco, A., Calise, G., and Bizzarri, N., 2017, "Development, Deployment and Experimental Test on the Novel Tethered System GEM for Tidal Current Energy Exploitation," *Renewable Energy*, **114**, pp. 323–336.
- [6] Mademlis, G., Liu, Y., Chen, P., and Singhroy, E., 2020, "Design of Maximum Power Point Tracking for Dynamic Power Response of Tidal Undersea Kite Systems," *IEEE Trans. Ind. Appl.*, **56**(2), pp. 2048–2060.

- [7] Loyd, M. L., 1980, "Crosswind Kite Power (for Large-Scale Wind Power Production)," *J. Energy*, **4**(3), pp. 106–111.
- [8] Vermillion, C., Grunnagle, T., Lim, R., and Kolmanovsky, I., 2014, "Model-Based Plant Design and Hierarchical Control of a Prototype Lighter-Than-Air Wind Energy System, With Experimental Flight Test Results," *IEEE Trans. Control Syst. Technol.*, **22**(2), pp. 531–542.
- [9] Williams, P., Lansdorp, B., and Ockels, W., 2007, "Modeling and Control of a Kite on a Variable Length Flexible Inelastic Tether," *AIAA Paper No. 2007-6705*.
- [10] Cobb, M. K., Barton, K., Fathy, H., and Vermillion, C., 2020, "Iterative Learning-Based Path Optimization for Repetitive Path Planning, With Application to 3-D Crosswind Flight of Airborne Wind Energy Systems," *IEEE Trans. Control Syst. Technol.*, **28**(4), pp. 1447–1459.
- [11] Olinger, D. J., and Wang, Y., 2015, "Hydrokinetic Energy Harvesting Using Tethered Undersea Kites," *J. Renewable Sustainable Energy*, **7**(4), p. 043114.
- [12] Li, H., Olinger, D. J., and Demetriou, M. A., 2019, "Modeling and Control of Tethered Undersea Kites," *Ocean Eng.*, **190**, p. 106390.
- [13] Fagiano, L., Huynh, K., Bamieh, B., and Khammash, M., 2013, "Sensor Fusion for Tethered Wings in Airborne Wind Energy," *American Control Conference*, Washington, DC, June 17–19, pp. 2884–2889.
- [14] Fredette, R., 2015, "Scale-Model Testing of Tethered Undersea Kites for Power Generation," *Master's thesis*, Worcester Polytechnic Institute, Worcester, MA.
- [15] Vermillion, C., Glass, B., and Szalai, B., 2014, "Development and Full-Scale Experimental Validation of a Rapid Prototyping Environment for Plant and Control Design of Airborne Wind Energy Systems," *ASME Paper No. DSCC2014-5907*.
- [16] Vermillion, C., Glass, B., and Greenwood, S., 2014, "Evaluation of a Water Channel-Based Platform for Characterizing Aerostat Flight Dynamics: A Case Study on a Lighter-Than-Air Wind Energy System," *AIAA Paper No. 2014-2711*.
- [17] Deodhar, N., Vermillion, C., and Tkacik, P., 2015, "A Case Study in Experimentally-Infused Plant and Controller Optimization for Airborne Wind Energy Systems," *American Control Conference*, Chicago, IL, July 1–3, pp. 2371–2376.
- [18] Deodhar, N., Bafandeh, A., Deese, J., Smith, B., Muyimbwa, T., Vermillion, C., and Tkacik, P., 2017, "Laboratory-Scale Flight Characterization of a Multitethered Aerostat for Wind Energy Generation," *AIAA J.*, **55**(6), pp. 1823–1832.
- [19] Cobb, M., Vermillion, C., and Fathy, H., 2016, "Lab-Scale Experimental Crosswind Flight Control System Prototyping for an Airborne Wind Energy System," *ASME Paper No. DSCC2016-9737*.
- [20] Cobb, M., Deodhar, N., and Vermillion, C., 2018, "Lab-Scale Experimental Characterization and Dynamic Scaling Assessment for Closed-Loop Crosswind Flight of Airborne Wind Energy Systems," *ASME J. Dyn. Syst., Meas., Control*, **140**(7), p. 071005.
- [21] Siddiqui, A., Ramaprabhu, P., Deese, J., and Vermillion, C., 2019, "Flight Dynamics and Control of a Farm of Tethered Energy Systems in a Turbulent Field," *ASME Paper No. DSCC2019-9168*.
- [22] Fossen, T. I., 1994, *Guidance and Control of Ocean Vehicles*, Wiley, New York.
- [23] Meirovitch, L., 2010, *Methods of Analytical Dynamics*, Dover, New York.
- [24] Thomson, W. T., 1986, *Introduction to Space Dynamics*, Dover, New York.
- [25] Wendel, K., 1956, *Hydrodynamic Masses and Hydrodynamic Moments of Inertia*, MIT Libraries, Cambridge, MA.
- [26] Drela, M., and Youngren, H., 2017, "XFOIL".
- [27] Yoder, C. D., Gemmer, T. R., and Mazzoleni, A. P., 2019, "Modelling and Performance Analysis of a Tether and Sail-Based Trajectory Control System for Extra-Terrestrial Scientific Balloon Missions," *Acta Astronaut.*, **160**, pp. 527–537.
- [28] Rapp, S., Schmehl, R., Oland, E., Smidt, S., Haas, T., and Meyers, J., 2019, "A Modular Control Architecture for Airborne Wind Energy Systems," *AIAA Paper No. 2019-1419*.
- [29] Stewart, E. A., 2017, *Design, Analysis, and Validation of a Free Surface Water Tunnel*, North Carolina State University, Raleigh, NC.
- [30] Otsu, N., 1979, "A Threshold Selection Method From Gray-Level Histograms," *IEEE Trans. Syst., Man, Cybern.*, **9**(1), pp. 62–66.
- [31] Kennedy, J., and Eberhart, R., 1995, "Particle Swarm Optimization," *Proceedings of International Conference on Neural Networks*, Vol. 4, Perth, WA, Nov. 27–Dec. 1, pp. 1942–1948.